



Additive manufacturing of highly reconfigurable plasmonic circuits for terahertz communications: supplement

YANG CAO, KATHIRVEL NALLAPPAN,  HICHEM GUERBOUKHA, GUOFU XU,  AND MAKSIM SKOROBOGATIY*

Department of Engineering Physics, École Polytechnique de Montréal, Montreal, Québec H3T 1J4, Canada
**Corresponding author: maksim.skorobogatiy@polymtl.ca*

This supplement published with The Optical Society on 31 August 2020 by The Authors under the terms of the [Creative Commons Attribution 4.0 License](#) in the format provided by the authors and unedited. Further distribution of this work must maintain attribution to the author(s) and the published article's title, journal citation, and DOI.

Supplement DOI: <https://doi.org/10.6084/m9.figshare.12685787>

Parent Article DOI: <https://doi.org/10.1364/OPTICA.398572>

Additive manufacturing of highly reconfigurable plasmonic circuits for terahertz communications: supplementary material

YANG CAO, KATHIRVEL NALLAPPAN, HICHEM GUERBOUKHA, GUOFU XU, AND MAKSIM SKOROBOGATIY*

Department of Engineering Physics, École Polytechnique de Montréal, Montreal, Québec, H3T 1J4, Canada
 *Corresponding author: maksim.skorobogatiy@polymtl.ca

Published XX Month XXXX

This document provides supplementary information to “Additive manufacturing of highly reconfigurable plasmonic circuits for terahertz communications,”

1. The influence of the accidental degeneracy of the dispersion relations of the SPP mode and bulk modes of a resin cage

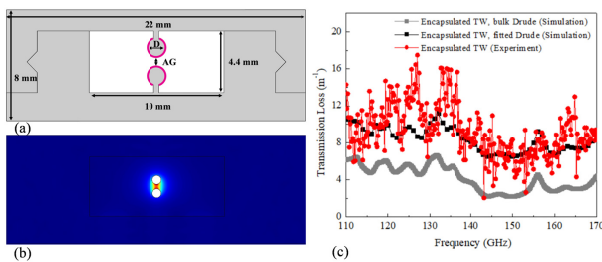


Fig. S1. (a). The schematic of a two-wire waveguide encapsulated by a resin cage featuring wider confined air area than the one indicated in the main-text. (b). The modal electric amplitude field distribution of the supported THz SPP wave at 140 GHz. (c). The theoretical modal loss (by field) of the THz SPP wave and the measured transmission loss (by field) of the straight two-wire waveguide.

Here we studied a straight two-wire waveguide encapsulated by a resin cage featuring a wider internal dimension (the width of the air space is increased from 6.5 mm to 10 mm) than that of the two-wire waveguide indicated in the main-text (see Fig. S1(a)). In these two designs, the geometries of the wire support including wire diameter and inter-wire separation are identical. As larger hollow space is left between the wires and the resin cage in this design, the presence of a portion of the supported THz SPP wave in the lossy resin is smaller than that of the

waveguide studied in the main-text (see Fig. S1(b)). Therefore, the computed modal loss and measured transmission loss (by field) of this waveguide are somewhat smaller at 140 GHz. However, Fig. S1(c) shows that the modal loss of the supported THz SPP wave in a broad spectral range 110-135 GHz is larger than that of the other characterized frequencies, and larger measured transmission loss appears in such spectral range in experiments. It is different from the two-wire waveguides indicated in main-text whose measured transmission loss maintains despite of the presence of modal loss peak of the supported THz SPP wave featuring a narrow spectral width in numerical simulations. We believe that the observed modal loss increase is resulting from the hybridization between the THz SPP wave and a mode supported by the resin cage. The spectral position of the resonant frequency is related to the geometry of wires and the cage. In this design (Fig. S1(a)), even with inaccuracy in 3D printed structure from the ideal model, the avoided crossing phenomenon is easy to be excited, thus resulting in the larger transmission loss in a broad spectral range. Therefore, different from the stand-alone two-wire waveguide that features a frequency-insensitive transmission loss, the proposed 3D printed waveguide has to be designed appropriately to avoid the presence of modal loss peaks featuring a large spectral width around the desired operation frequency.

2. The transverse electric field distribution of the fundamental modes of micro-encapsulated two-wire waveguides and WR6.5 waveguide flange

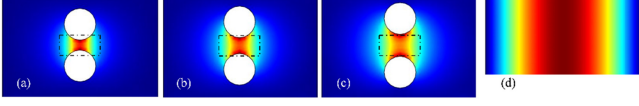


Fig. S2. The transverse modal electric field distribution $|E_t|$ of the fundamental mode of the micro-encapsulated two-wire waveguides featuring different inter-wire separations at 140 GHz. The black dotted region represents the opening of the WR6.5 waveguide flange under the butt-coupling arrangement. (a) $AG=0.5*hzWR6$. (b) $AG=0.8*hzWR6$. (c) $AG=1.1*hzWR6$. (d) The transverse modal electric field distribution $|E_t|$ of the fundamental mode of the WR6.5 waveguide flange at 140 GHz.

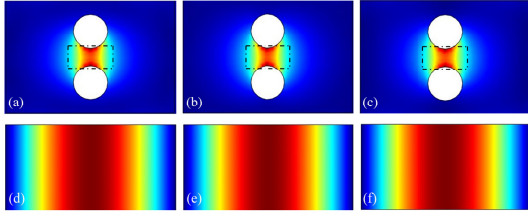


Fig. S3. The transverse electric field distribution $|E_t|$ of the fundamental mode of a micro-encapsulated two-wire waveguide at

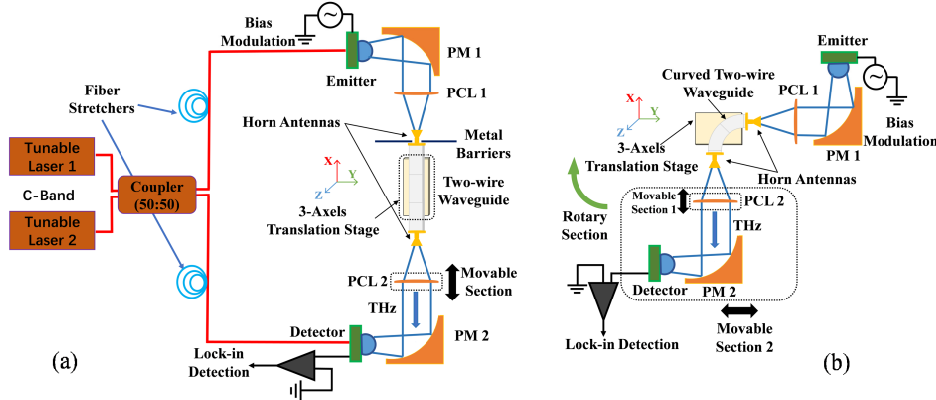


Fig. S4. (a). The experimental setup to measure the propagation loss and the GVD of straight two-wire waveguides. The same setup is also used to characterize the two-wire waveguide Bragg gratings. PM: off-axis parabolic mirror featuring a reflective focal length of 10.1 cm (MPD249-M01, Thorlabs, Inc.), PCL: PTFE plano-convex lens featuring a focal length of 7.5 cm (LAT075, Thorlabs, Inc.). (b). The experimental setup to measure the bending loss of the curved two-wire waveguides.

3.1 The measurement of the propagation loss and GVD of the straight two-wire waveguides and the characterization of the waveguide Bragg gratings (WBGs)

The straight two-wire waveguides were characterized in the following processes. Firstly, the reference spectrum was recorded by placing two WR6.5 conical horn antennas (Virginia Diode, Inc.) between the two neighboring plano-convex lenses PCL1 and PCL2 with their focal points at the input and output plane of the connected waveguide flanges. Note that PCL2 is mounted onto an optical rail, and represents a movable section (MS) of the spectrometer, thus allowing measuring two-wire waveguides of various lengths, as well as the reference signal. The assembled two-wire waveguide composed of multiple waveguide sections (WSs) was connected with WR6.5 conical horn antennas at its both ends. The whole section was then inserted into the spectrometer with the input and output planes of the waveguide flanges at the focal points of PCL1 and PCL2 via

the operation frequencies of (a) 110 GHz (b) 140 GHz and (c) 170 GHz. The transverse modal electric field distribution $|E_t|$ of the TE_{10} mode of the WR6.5 waveguide flange at the operation frequencies of (d) 110 GHz (e) 140 GHz and (f) 170 GHz.

3. The characterization of the micro-encapsulated two-wire waveguide components and circuits

The proposed 3D printed micro-encapsulated two-wire waveguide components and circuits were studied by using the CW-THz spectroscopy system (TOPTICA Photonics) [1,2]. The schematic of the experimental setup is shown in Figs. S4(a), S4(b), S6(a), S6(b) and S7(a). The CW-THz spectroscopy system is briefly explained as follows. Two distributed feedback (DFB) lasers of power ~ 30 mW, operating in the infrared C-band with slightly different emission wavelengths are used as the source of THz generation. A 50:50 fiber coupler is used to combine the two laser beams and split into both emission and detection arms respectively. The THz radiation is generated in the emitter photomixer (under bias voltage) and corresponds to the beat frequency between the two DFB lasers. The output THz frequency can be varied by simply tuning the emission wavelengths of the lasers. A similar photomixer (without bias voltage) and a lock-in amplifier are used to detect the THz radiation. The focused linear-polarized CW-THz beam transmitting through the waveguides is re-collimated and the amplitude of the THz signal is recorded using lock-in detection.

adjusting the positions of MS and 3-axels translation stage. The schematic of the characterization setup is shown in Fig. S4(a). Finally, a cutback measurement was carried out by subsequently removing the WSs sandwiched between the input and output WSs. The measured complex transmission spectra (by field) was then analyzed to estimate the transmission loss and coupling loss of the two-wire waveguide.

In experiments, two sets of waveguide samples were characterized to distinguish the transmission loss α_{st} and the coupling loss Cl (by field) between neighboring WSs. Each set includes a same number of WSs with the same length l . By comparing the measurements with the reference, the normalized transmittance (by field) t_{ml} of waveguides can be given as follow:

$$t_{ml} = |C_{in}| |C_{out}| Cl^{m-1} \cdot \exp(-\alpha_{st} ml) \quad (S1)$$

where, $|C_{in}|$ and $|C_{out}|$ refer to the input and output field coupling coefficients which are assumed as a constant, while

m refers to the number of measured WSs. By expressing the Eq. (S1) as the logarithms of e and comparing the transmittance of two waveguides integrated by the same number of sections from different sets of samples, the transmission loss α_{st} was derived by the following equation,

$$\log(t_{m_1}) - \log(t_{m_2}) = -m\alpha(l_1 - l_2) \quad (S2)$$

Then, with the measured transmission loss α_{st} , the average coupling loss Cl was obtained by comparing the transmittance of waveguides exhibiting different lengths.

The phase measurement was performed by the CW-THz spectroscopy using an optical delay line in the form of polarization-maintaining fiber wound piezoelectric elements (see Fig. S4(a)) [3]. The effective RI of the two-wire waveguide was computed from the normalized complex transmission spectrum (by field) and then fitted into a two-order polynomial function of angular frequency ω [4]. The GVD was computed as the second order derivative of the derived waveguide propagation constant with respect to ω by Eq. (3).

To characterize the two-wire waveguide Bragg gratings, a 3D printed two-wire waveguide with slits (the schematic diagram is shown in Fig. 4(a)) was placed with its two ends at the focal points of the PCL1 and PCL2. Firstly, the reference transmission spectrum (by field) was obtained by measuring the waveguide without the paper. After inserting the paper-based periodic metalized structure between wires, the transmission spectra (by field) of WBGs were recorded. The transmittances spectra were then obtained by dividing them by the reference data.

3.2 The measurement of the bending loss of the two-wire waveguide bends

The transmission spectra of the two-wire waveguide bends were measured by the following process. 90° bends having different bend radiuses were fabricated and characterized. In order to avoid the difference in the coupling coefficient between different waveguide bends with the WR6.5 waveguide flange, a 5mm-length straight WS is integrated at both ends of each waveguide bend. The schematic of the experimental setup is shown in Fig. S4(b). It is noted that the straight waveguide can be measured by simply rotating the rotary section clockwise by 90° from its original position. Firstly, the reference transmission spectrum of a straight waveguide whose length is same with the curved waveguide was measured. Next, the transmission spectrum of the curved two-wire waveguide with the axis of rotation parallel to the line connecting wire centers was measured by resetting the rotary section (see Fig. S4(b)). Similarly, the curved waveguides with axis of rotation perpendicular to the line connecting wire centers was measured by rotating the emitter and detector photomixers by 90°. Therefore, the polarization state of the THz light that was launched into two-wire waveguides was maintained for all the measurement.

In order to derive the bending loss a_b from the experimental results, the power coupling coefficient $|C(R)|^2$ between straight and bent waveguide was computed using mode matching method (the results are shown in Fig. 3(e)) [5]. Additionally, given the high similarity in the modal field distribution of the THz SPP wave supported by the bent and straight waveguides (see Figs. 1(d), 3(a), and 3(b)), the power coupling coefficient between two bent WSs is assumed identical to the one between two straight WSs.

Therefore, the bending loss α_b of waveguide bends can be extracted by comparing the measured transmission spectrum of the bend with that of the corresponding straight waveguides using,

$$\alpha_b = -\log\left(t_{curve} / t_{straight} / |C(R)|^2\right) / (0.5\pi R) \quad (S3)$$

where, R refers to the bend radius of the waveguide bends, t_{curve} and $t_{straight}$ refer the transmittance (by field) of the curved and straight waveguides.

4. The theoretical analysis of a two-wire WBG

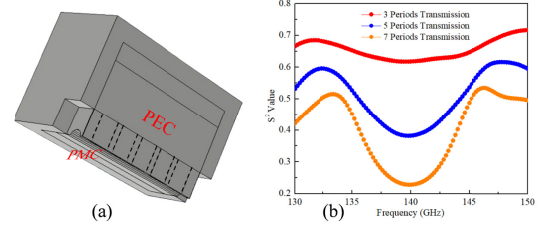


Fig. S5. (a) The 3D model of a two-wire waveguide Bragg grating to estimate the transmission and reflection coefficients using COMSOL Multiphysics. (b) The simulated power transmission $|S_{21}|^2$ for WBGs with different number of periods.

In this section, we study both theoretically and numerically a two-wire WBG with the Bragg frequency of ~140 GHz. Theoretically, using Eqs. (7) and (9) with m_w of 0 and m_p of 3, the total period width of WBG and the width of section 2 in one period (see Fig. 4(b) I) are set as 3.21 mm and 2.46 mm respectively to realize the Bragg resonance at 140 GHz. WBGs featuring such design were numerically studied using COMSOL Multiphysics by 3D models. (The geometry of a WBG consisting five periods is shown in Fig. S5(a)). The derived spectral position of the transmission dip is at 140 GHz (see Fig. S5(b)), which agrees well with the theoretical results obtained by using Eqs. (7) and (9).

5. The characterization of two-wire waveguide-based THz coupler

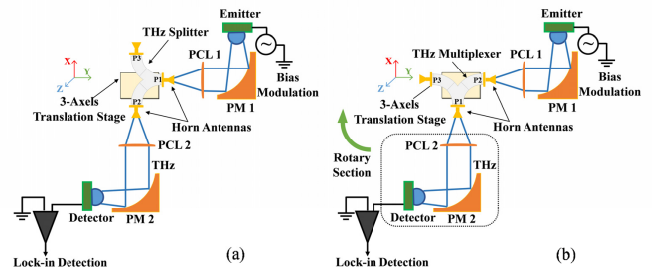


Fig. S6. The experimental setup to characterize (a) THz splitter. (b) THz multiplexer.

The two-wire waveguide-based THz coupler containing three ports was characterized by the following processes. Firstly, each port of the THz coupler was connected with a WR6.5 conical horn antenna. When functioning as a THz splitter, the coupler was inserted into the CW-THz spectrometer system with the input and output planes of waveguide flanges connected with ports 1 and 2 at the focal points of PCL1 and PCL2 (see Fig. S6(a)). The transmission spectrum received at the output port 2 was recorded when the THz light was launched into the port 1. Then, the THz splitter was turned over to measure the transmission spectrum at the output port 3. When functioning as a THz multiplexer, the coupler was placed with the input and

output planes of waveguide flanges connected with ports 2 and 1 at the focal points of PCL1 and PCL2 (see Fig. S6(b)). The transmission spectrum received at the output port 1 was recorded when the THz light was launched into the port 2. Then, by clockwise rotating the rotary section by 90°, the transmission spectrum at port 3 was measured. To estimate the amount of THz power that is coupled into the input port, the THz coupler was then replaced by a straight waveguide and the transmission spectrum was measured with the same incident THz light (see Fig. S6(b)) (The measurement process is detailed in Supplementary Material 3.1). The reference spectrum (i.e. the maximum amplitude of the coupled THz light) was derived from this transmission spectrum by,

$$t_{\text{ref}} = t_{\text{straight}} / \exp(-\alpha_{\text{st}} I_{\text{straight}}) / Cl \quad (\text{S4})$$

Additionally, the transmission spectrum of a two-wire waveguide bend featuring the same geometry of half of a THz coupler (see Fig. 4(b)) was chosen as a control of that of the THz coupler. The transmission spectrum of the waveguide bend was measured with the same incident THz light (the process is detailed in supplementary material 3.2).

6. The characterization of two-wire waveguide-based Add-Drop Multiplexer (ADM)

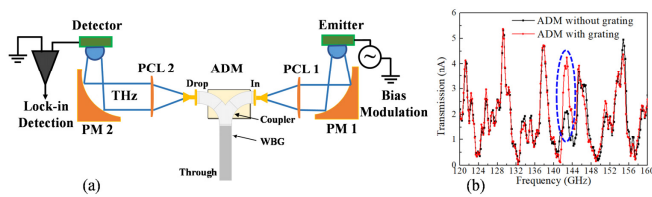


Fig. S7. (a). The experimental setup to characterize the THz ADM. (b) Transmission amplitude of the ADM with and without paper-based metalized periodic pattern inserted into the integrated WBG.

The characterization of the ADM was carried out as follows. Firstly, the THz coupler and WBG were assembled using the interconnects at the end facets of both waveguide components. Then, two WR6.5 conical horn antennas were connected to the In and Drop ports. The schematic of the experimental setup is shown in Fig. S7(a). When the THz light was launched into the In port, the transmission spectra received at the Drop port with and without the paper-based metalized periodic structure inserted into the WBG were measured (see Fig. S7(b)). For the purpose of clarity, the data points within the blue circle showing the resonance peak is presented in Fig. 6(c).

References

1. A. Roggenbuck, H. Schmitz, A. Deninger, I. C. Mayorga, J. Hemberger, R. Güsten, and M. Grüninger, "Coherent broadband continuous-wave terahertz spectroscopy on solid-state samples," *New J. Phys* **12**(4), 043017 (2010).
2. D. Stanze, A. Deninger, A. Roggenbuck, S. Schindler, M. Schlak, and B. Sartorius, "Compact CW terahertz spectrometer pumped at 1.5 μm wavelength," *J. Infrared Millim. Terahertz Waves* **32**(2), 225–232 (2011).
3. A. Roggenbuck, K. Thirunavukkuarasu, H. Schmitz, J. Marx, A. Deninger, I. C. Mayorga, R. Güsten, J. Hemberger, and M. Grüninger, "Using a fiber stretcher as a fast phase modulator in a continuous wave terahertz spectrometer," *JOSA B* **29**(4), 614-620 (2012).

4. H. Guerboukha, K. Nallappan, and M. Skorobogatiy, "Toward real-time terahertz imaging," *Adv. Opt. Photonics* **10**(4), 843–938 (2018).
5. M. Skorobogatiy, *Nanostructured and Subwavelength Waveguides: fundamentals and applications* (JWS, 2012).